applied sciences

MDPI

Article

Comparative Analysis of the Effect of Rotor Faults in the Performance of Low-Speed High-Torque Machines

Carlos Madariaga-Cifuentes [1], Cesar Gallardo [1,2], Jose E. Ruiz-Sarrio [3], Juan A. Tapia [1] and Jose A. Antonino-Daviu [3,*]

[1] Department of Electrical Engineering, University of Concepcion, Concepcion 4070386, Chile; carlosmadariaga@udec.cl (C.M.-C.); cesar.gallardosanchez@nottingham.ac.uk (C.G.); juantapia@udec.cl (J.A.T.)
[2] Power Electronics, Machines, and Control Research Institute, University of Nottingham, Nottingham NG7 2RD, UK
[3] Instituto Tecnológico de la Energía, Universitat Politècnica de València, 46022 Valencia, Spain; joruisar@die.upv.es
* Correspondence: joanda@die.upv.es

Abstract: Several studies have focused on modeling and analyzing the impact of rotor faults in conventional low-pole-count machines, while related research on low-speed high-torque (LSHT) machines with a high pole count remains limited. In these machines, the combination of low speed, high inertia, and high torque levels presents a critical application for advanced diagnosis techniques. The present paper aims to describe and quantify the impact of rotor faults on the performance of LSHT machine types during the design stage. Specifically, 10-pole and 16-pole synchronous reluctance machines (SynRMs), permanent magnet synchronous machines (PMSMs), and squirrel-cage induction machines (SCIMs) are assessed by means of detailed 2D simulations. The effects of eccentricity, broken rotor bars, and partial demagnetization are studied, with a focus on performance variations. The results show that LSHT PMSMs are not significantly affected by the partial demagnetization of a few magnets, and the same holds true for common faults in SynRMs and SCIMs. Nonetheless, a significant increase in torque ripple was observed for all evaluated faults, with different origins and diverse effects on the torque waveform, which could be hard or invasive to analyze. Furthermore, it was concluded that specialized diagnosis techniques are effectively required for detecting the usual faults in LSHT machines, as their effect on major performance indicators is mostly minimal.

Keywords: condition monitoring; finite-element evaluation; low-speed high-torque applications

check for updates

Received: 26 December 2024
Revised: 5 February 2025
Accepted: 6 February 2025
Published: 8 February 2025

Citation: Madariaga-Cifuentes, C.; Gallardo, C.; Ruiz-Sarrio, J.E.; Tapia, J.A.; Antonino-Daviu, J.A. Comparative Analysis of the Effect of Rotor Faults in the Performance of Low-Speed High-Torque Machines. *Appl. Sci.* **2025**, *15*, 1721. https://doi.org/10.3390/app15041721

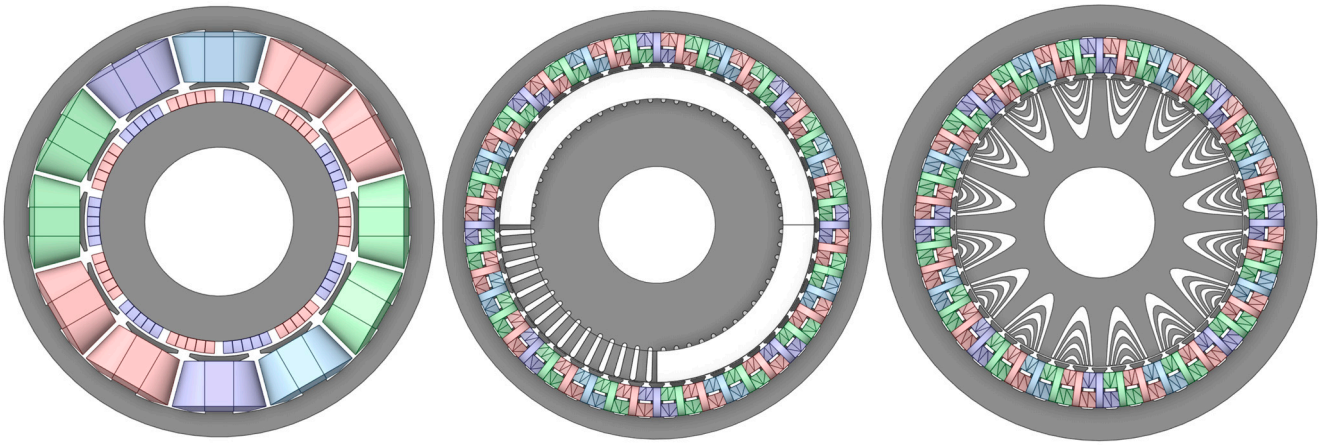
Copyright: © 2025 by the authors. Licensee MDPI, Basel, Switzerland. This article is an open access article distributed under the terms and conditions of the Creative Commons Attribution (CC BY) license (https://creativecommons.org/licenses/by/4.0/).

1. Introduction

Currently, there are more than 300 million electric motors worldwide, which account for nearly 40% of global electricity demand [1]. Their maintenance accounts for a significant percentage of production costs: in the petrochemical industry alone, it is estimated that maintenance costs represent between 15% and 40% of the total production cost [2]. More specifically, the costs associated with maintenance depend on its nature, as indicated in industrial surveys [3–6], with predictive maintenance having the best cost–benefit. However, many industries still rely on preventive and corrective maintenance, considering the challenges and initial costs related to the development of technology for frequent monitoring/testing of the equipment and the creation of algorithms for early problem detection [7].

In some industries, it is often assumed that common faults can be readily detected through basic diagnostics, following a preventive maintenance strategy [8]. In contrast, many major electromagnetic and mechanical faults are not easily detectable and are triggered by earlier non-destructive phenomena [9–11]. These earlier indicators are difficult to detect using simple monitoring metrics but can be easily detected with the appropriate diagnostic technique. Moreover, several factors could influence the invisibility of faults and the lack of influence on the machine performance metrics: the type of fault, machine topology, and dimensions, among other parameters [12].

The above is particularly relevant for low-speed high-torque (LSHT) machines, which are less susceptible to excessive vibration due to their operating speed [13] and robust mechanical response. LSHT applications have been dominated by permanent magnet synchronous machines (PMSMs, shown in Figure 1a), given their high torque density, efficiency, and power factor [14–16]. Nonetheless, and emanating from rare-earth dependance concerns, increased attention has been brought to improving the performance of alternative LSHT drive systems used in industrial applications. Among them, high-pole-count induction motors (IMs, presented in Figure 1b) have been investigated, offering moderate performance [17,18], as well as synchronous reluctance machines (SynRMs, sketched in Figure 1c) [19], providing high efficiency but a poor power factor.



(**a**) (**b**) (**c**)

Figure 1. LSHT machines in 3D sketches: (**a**) example of LSHT PMSM with 14 poles; (**b**) example of LSHT SCIM with 16 poles; (**c**) example of LSHT SynRM with 16 poles. The three-phase windings are highlighted in red, green, and blue for phases A, B, and C, respectively.

In these machines, the combination of low speed, high inertia, and high torque levels constitutes a critical application for advanced diagnosis techniques. In this regard, there is an opportunity to showcase the actual effects of the usual faults in the performance of LSHT machines, an area that has not been extensively addressed in the literature. In contrast, several studies have focused on modeling and analyzing the impact of faults in conventional low-pole-count PMSMs [20–22], SynRMs [23–25], and IMs [26–29], while related research on LSHT machines remains limited.

Some literature addresses the impact of the usual faults on LSHT machines, particularly for large wound rotor synchronous generators (WRSGs) [30–32]. However, there is limited research on other LSHT machine topologies such as PMSMs, and there is a lack of studies on LSHT IMs and SynRMs. The existing literature on LSHT PMSMs primarily focuses on the impact of eccentricity faults in high-pole-count radial flux (RF) PMSMs [33], axial flux (AF) PMSMs [34,35], and PMSMs with tooth-coil winding (TCW) [36]. Also, partial demagnetization has been analyzed [37]. In [33], an eight-pole and a twenty-four-pole PMSM were evaluated in the presence of rotor eccentricity. The results showed little

difference in the magnitudes of the new components introduced by the static and dynamic eccentricity for the same machine. However, the negative effects of rotor eccentricity in high-pole fractional-slot PMSMs were found to be more than twice that in integer-slot PMSMs with a lower pole count, in terms of unbalanced electromagnetic forces. In [34], a 28-pole 2.2 kW AF-PMSM was evaluated by means of detailed 3D FE analysis, considering static inclined eccentricity. The study examined the effects on airgap flux, back-emf, axial forces, and uneven forces, concluding that static eccentricity deforms airgap magnetic fields and generates unbalanced magnetic force (UMF). This UMF leads to continuous torque acting on the bearings, resulting in additional mechanical load, vibration, and acoustic noise. These findings led to increased interest in modeling static inclined eccentricity, which was addressed in [35] through a magnetic field calculation approach that evaluates static inclined eccentricity in AF-PMSMs, though it is also applicable to RF-PMSMs. This method effectively estimates slight changes to the spatial flux density distribution caused by eccentricities. Related research on special modular PMSMs with TCW can be found in [36], which further evaluates the effect of both static and dynamic eccentricity on the performance of these machines. The study found that while mean torque and back-emf are not substantially impacted by eccentricity, cogging torque and radial forces are significantly affected, which is concordant with [34,35]. In turn, partial demagnetization is addressed in [37], where a 42-pole LSHT-PMSM was analyzed through the finite element method (FEM) under various degrees of demagnetization. The study observed differences in the harmonic content of the torque waveform, though the effect was minimal, highlighting the need for advanced diagnosis techniques for fault detection.

From the above, it should be noted that high-pole-count WRSGs and LSHT PMSMs, particularly those with the AF topology, have been addressed in the literature. Nevertheless, to the best of the authors' knowledge, there is no research focusing on the impact of the usual faults on the performance of high-pole-count IMs or SynRMs, despite several design proposals for these machines being available in the literature [17–19], along with off-the-shelf 12-pole machines used in special applications. Furthermore, although it is widely accepted that these faults often go unnoticed during routine inspections, the literature has yet to quantify the extent to which topology-specific parameters influence fault sensitivity in LSHT machines, particularly in a comparative context.

This paper aims to describe and demonstrate the impact of the usual faults in the performance of several LSHT machines using a numerical approach. Squirrel-cage IMs, SynRMs, and PMSMs are designed, optimized, and analyzed in this study with two objective speeds, based on detailed finite element simulations to isolate phenomena related to the faults. Also, the study covers several machine topologies and their specific faults, in order to underline the need for advanced diagnostic techniques oriented to each machine topology. The remainder of the paper is organized as follows. Section 2 describes the usual faults in conventional machines and provides a more detailed and focused literature review, including PMSMs, SCIMs, and SynRMs. Section 3 presents the methodology of machine design and analysis using FE simulations, also describing the theoretical background. Sections 4 and 5 provide the results of the assessment, considering the raw performance evaluation in faultless conditions in Section 4, and the impact of the usual faults in Section 5. Finally, Section 6 outlines the main findings and general remarks of this work.

2. Usual Rotor Faults in Conventional Machines

Electrical machines are susceptible to different faults depending on their rotor and stator structure, as different topologies feature different active structures that can be prone to specific faults. This section identifies and describes common faults shared by IMs, SynRMs, and PMSMs, as well as faults specific to each of these topologies.

2.1. Faults Shared by Conventional Machines—Unbalance, Misalignment, Eccentricity

Among the common faults for all topologies, eccentricity and misalignment are the focus of diagnosis research [12]. The eccentricity between rotor and stator is related to the uneven airgap along one mechanical rotation. Eccentricity possesses a different nature depending on the position of the minimum airgap. The eccentricity is static when the minimum airgap position is always fixed along the airgap periphery, as depicted in Figure 2b. This is normally caused by inherent mounting or manufacturing imperfections. On the other hand, dynamic eccentricity takes place when the minimum airgap position depends on the instantaneous rotor position (i.e., dynamically changes with rotating frequency), as illustrated in Figure 2c. Some frequent causes for dynamic eccentricity are rotor ovality and bearing misalignment.

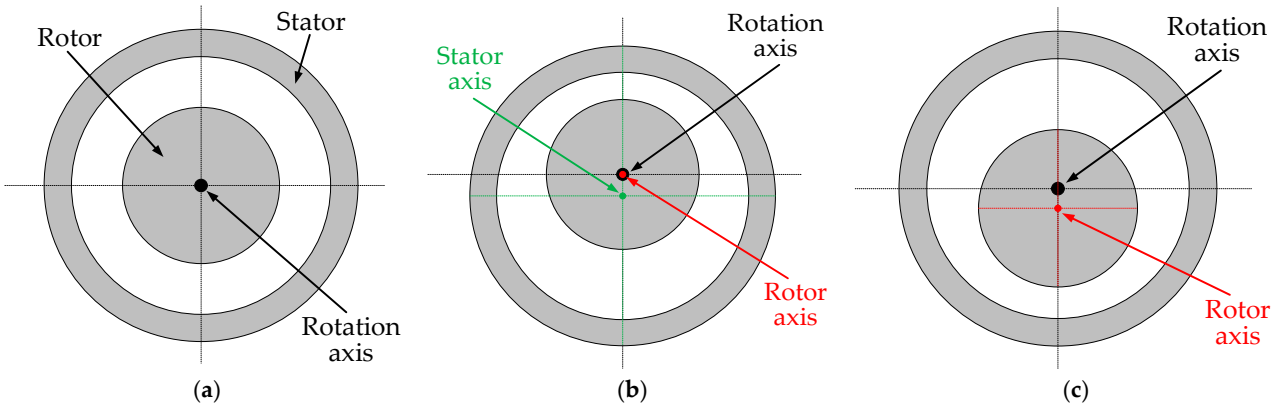


Figure 2. Different eccentricity types in electric machines: (**a**) faultless machine; (**b**) machine with static eccentricity; (**c**) machine with dynamic eccentricity.

Mixed eccentricity combines both static and dynamic cases and represents the most common practical scenario. The eccentricity condition is inherent to all machines and, thus, low eccentricity levels are normally accepted up to 10% of the airgap thickness [38].

In turn, misalignment refers to the positional deviation between the rotational axes of two coupled shafts. This misalignment can induce rotor–stator relative displacement, analogous to the effects observed in eccentricity. The misalignment is defined in two planes and in two modes. The parallel misalignment occurs when the rotational axes of two coupled shafts are parallel but not collinear, as shown in Figure 3b. Angular misalignment takes place when the rotational axes of two coupled shafts intersect but are not parallel, as illustrated in Figure 3c. This means that the shafts are angled relative to each other, resulting in a situation where the shafts are closer together at one end and further apart at the other. The combination of parallel and angular misalignment can also occur in real cases, further increasing the additional forces on rotors, bearings, couplings, and seals.

The acceptable levels of shaft misalignment depend on the nominal rotating speed and the utilized mechanical coupling, as well as on the type of load [39]. Different misalignment modes are related to eccentricity indicators since they induced a relative rotor–stator displacement [40].

The unbalance fault derives from the mass uneven distribution in rotating components such as the coupling or the driven load. It results in the generation of unbalanced centrifugal forces and moments, which can potentially damage various machine components. It is closely associated to the dynamic eccentricity case since it induces a rotating relative displacement between stator and rotor [41].

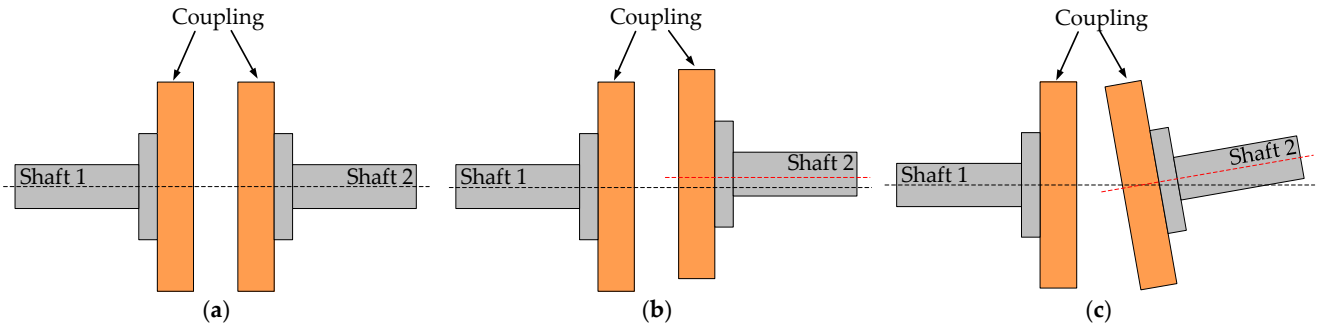


Figure 3. Different misalignment types: (**a**) reference faultless machine; (**b**) parallel misalignment; (**c**) angular misalignment.

In summary, from an electromagnetic perspective, common faults related to inherent eccentricity, misalignment, and unbalance faults can be converted to the analysis of static, dynamic, and mixed eccentricity.

2.2. PMSM Faults: Demagnetization

Permanent magnet synchronous machines (PMSMs) are widely used in LSHT applications, relying on a high pole count and strong rare-earth magnets to provide high torque density [42–44]. Moreover, pairing the features of PMSMs with the adoption of tooth-coil winding (TCW) configurations has proven to provide several advantages over the distributed winding (DW) counterparts [45]: short end-winding turns, low cogging torque, compactness, and a high copper space factor, which makes it possible to improve the machine power/weight ratio.

Nevertheless, the PMSM rotor can suffer from rotor irreversible demagnetization, which can lead to performance penalizations. This arises as a combination of various phenomena of a thermal, electrical, and mechanical nature. The uniform demagnetization (UD) case is described as the even demagnetization of all rotor magnets where only an amplitude decrease in the airgap flux density is observed [46]. The most likely reason for uniform demagnetization in all poles is the operation at excessive temperature. On the other hand, partial demagnetization (PD) can arise from different phenomena such as a combination of high temperature operation and demagnetizing MMF applied in the *dq* rotating stator frame. Figure 4 compares the magnetic flux distribution of UD and PD, respectively.

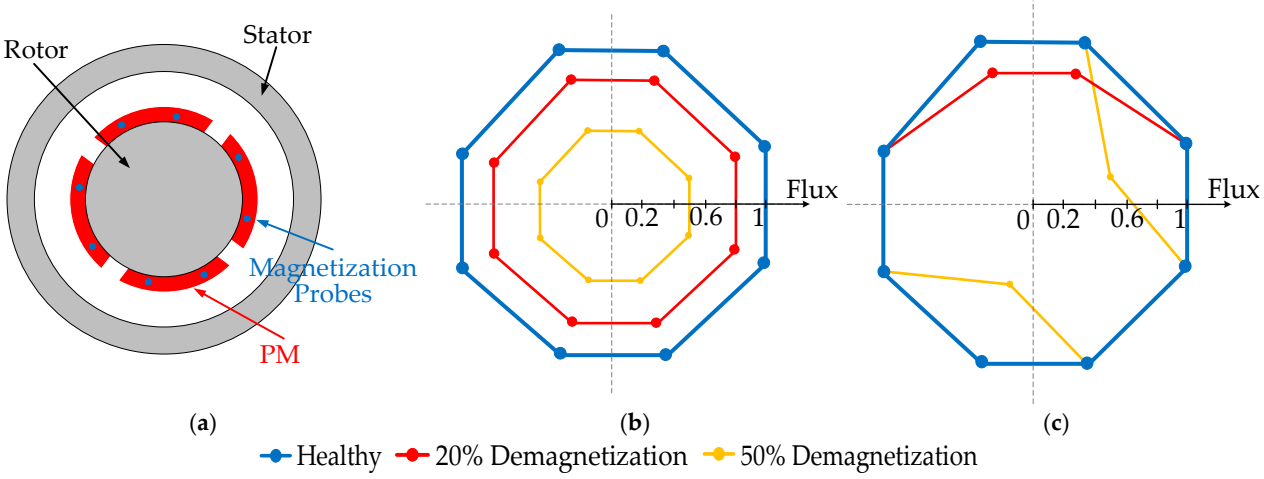


Figure 4. Types of demagnetization in electrical machines: (**a**) position of magnetization probes; (**b**) machine with uniform demagnetization; (**c**) machine with partial demagnetization.

A common case of partial demagnetization is the so-called trailing edge demagnetization which occurs at the edges of the magnets opposite to the direction of rotation [47]. This is accentuated for motors operating with a high load angle (i.e., the difference between the stator magnetic axis and the rotor q-axis). All demagnetization cases dramatically affect the PMSM performance. Furthermore, undetected demagnetization in its early stages can rapidly escalate the severity of failure. This progression is attributed to the resultant increased current consumption, which leads to higher joule losses and a subsequent rise in temperature within the coils and magnets.

2.3. SCIM Faults: Broken Rotor Bars

The SCIM represents the largest kind of motor technology used in the industry, playing a key role in the production process. SCIM technology is known for its ruggedness, efficiency, and relatively low cost when compared to other competitive topologies [48,49]. SCIMs are still considered the industry "work horse" as they dominate the electrical machine market in industrial applications. The SCIM is the cheapest and the most reliable machine topology based on mature manufacturing processes.

Nonetheless, the rotor circuit of these machines, which represents the weakest rotor element, is formed by copper or aluminum bars of different shapes, which are crafted and rotor-embedded by using different manufacturing technologies. It is well acknowledged that the broken rotor bar fault has increased occurrence likelihood in large motors starting under large inertia conditions with frequent start–stop operations (i.e., a frequent scenario in the mining industry) [50]. Some works link this failure to the combination of mechanical fatigue and thermal excess due to these frequent starts, which normally affects the stress concentrators such as the ring–bar connections and manufacturing imperfections [51]. The severity of the fault is quantified according to the number of broken rotor bars. In addition, the fault signature and, thus, its overall impact depend on the rotor magnetic asymmetry defined by the periodicity of the broken bars over the full rotor pitch [52].

2.4. SynRM Faults

Synchronous reluctance machines (SynRMs) have gained increasing attention in the past decade, especially in applications where enhanced efficiency and cost-effective power conversion is required [53]. When compared with the widely used induction motors (IMs), the absence of rotor windings in SynRMs leads to lower rotor losses and higher efficiency for the same frame size. Additionally, SynRMs are proposed as a rare-earth magnet-free technology with a lower cost than PMSMs [54]. Moreover, they are highly reliable, robust, and easy to maintain. Nevertheless, they have two critical disadvantages with an impact on their competitivity as stated in the literature: the high torque ripple and the low power factor [55].

From a diagnosis perspective, the absence of the rotor field and circuit represents a significant advantage. Nevertheless, the thickness of the rotor flux barriers should withstand the speed and stress requirements of the application at hand to avoid catastrophic failure [56]. The diagnosis and reliability of SynRM rotors have received limited research attention, since these are only subjected to common rotor faults such as eccentricities, misalignment, and mass unbalances [57]. However, misalignments and eccentricities faults induce a variation in the reluctance path and may influence the machine performance by altering the produced reluctance torque [57].

2.5. Remarks on the Influence of the Control Methodology and Actuation

Thermal and mechanical rotor stresses heavily depend on the start–stop period and on the driven load, which are smoothed by using inverters or soft-starters. Thus, the actuation method during repeated start–stop operations directly affects the rotor fault likelihood.

Note that PMSMs and SynRMs are normally fed by an inverter since they lack self-starting capabilities in their basic configuration [58]. The worst-case scenario is thus found for line-started induction motors with repeated start–stops and a high inertia load, which operate at an increased starting current and temperature. The analysis of faults' impact on LSHT line-started IMs, nonetheless, has not been yet addressed in the literature.

3. Methodology and Theoretical Background

As mentioned earlier, this paper aims to describe the impact of common faults in LSHT IMs, SynRMs, and PMSMs. This section describes the method used to design LSHT machines through multi-objective optimization, as well as the methodology used to assess the impact of common faults on these machines.

3.1. Designing LSHT Machines via Multi-Objective Optimization

The design optimization of electrical machines involves the trade-off of multiple objectives. A multi-objective optimization framework can be employed to identify the best solutions within a complex design space. Typically, a Pareto front is used to visualize the best trade-off solutions for the optimization problems.

The initial stage of the optimization process involves the parametrization of the machine model to enable its automation. In this study, the model's parameters are defined based on geometric data and dimensions, with constraints applied to ensure the feasibility of the proposed designs. Typical performance objectives are considered in this paper, including maximizing the electromagnetic torque, efficiency, and power factor, while minimizing the torque ripple. Additionally, factors such as cost reduction, material constraints, or restricted volume may be also considered. Each objective is mathematically formulated to facilitate quantitative evaluation during the optimization process. Design constraints, including limitations on size, material properties, or manufacturing feasibility, are also explicitly defined. The objectives and constraints defined for this analysis are summarized in Table 1 for all considered LSHT topologies.

Table 1. Objectives and constraints defined for the optimization process.

Parameter	Symbol	Units	PMSM	SynRM	SCIM
Mean Torque	T_{mean}	Nm	maximize	maximize	maximize
Torque Ripple	T_{rp}	%	minimize	minimize	minimize
Efficiency	η	%	maximize	maximize	maximize
Power Factor	$\cos\phi$	-	maximize	maximize	maximize
Current Density	J_{rms}	A/mm^2	$3-5$	$3-5$	$3-5$
Phase Voltage	$V_{ph,\ rms}$	V	$=220$	$=220$	$=220$
Volume	-	m^3	$=0.05$	$=0.05$	$=0.05$
Rated losses	-	W	$\cong 2500$	$\cong 2500$	$\cong 2500$

The considered current density range falls within the typical recommendations found in the literature for passive-cooled machines [59], though it can be adjusted if a more advanced thermal solution is applied. Phase voltage is selected following a typical available low-voltage source of 380 V_{rms} and a star connection. The volume constraint was chosen to match the dimensions of a standard 12-pole 45-kW SCIM. Rated losses were estimated through a preliminary thermal evaluation considering the maximum heat dissipation of

a 0.05 m^3 case in passive-cooling scenarios, which was also cross-referenced with catalog data for off-the-shelf low-speed motors.

To solve the optimization problem, an appropriate multi-objective optimization algorithm must be selected. Popular choices include genetic algorithms (GAs), particle swarm optimization (PSO), and the non-dominated sorting genetic algorithm II (NSGA-II). The algorithm selection is guided by the specific problem characteristics and the desired balance between computational efficiency and solution quality. However, in machine learning and optimization, it can be concluded from the well-known no-free-lunch-theorem that for certain types of problems the averaged computational cost for finding a solution over all problems of that type is the same for any optimization technique [60]. For this analysis, a multi-objective genetic algorithm (MOGA) is selected, also adopted and preferred in other related works [61]. The number of initial samples is set to correctly map the input parameters, and the number of designs evaluated per iteration is selected as a fraction of this initial population. In this paper, the fitting of each design is obtained using detailed 2D FE simulations with the semi-analytical processing of copper losses and end-winding effects, allowing fast design evolution.

In this work, two pole numbers are evaluated to analyze the effects of the usual faults in machines: 10-pole and 16-pole machines. The 10-pole configuration is closer to commercial machines, while the 16-pole configuration is unconventional and falls better into the low-speed category, in line with the existing literature on LSHT machines.

3.2. Fault Assessment in Selected LSHT Machines

In this work, fault assessment is carried out using detailed FE simulations in order to isolate related phenomena and discard the interference of mechanical or manufacturing deviations.

3.2.1. Unbalance, Misalignment, and Eccentricity

Unbalances and misalignments are typically treated as eccentricity in FE simulations, where the eccentricity is quantified based on the variations in the airgap length.

The airgap length (δ) in the absence of eccentricity is expressed as follows:

$$\delta(\theta_s) = \delta_0 \tag{1}$$

where θ_s is the coordinate angle (mechanical degrees) referenced in the stator frame, and δ_0 is the original faultless airgap length.

When static eccentricity is considered, the airgap length can be expressed as a function of θ_s, and is given by the following:

$$\delta(\theta_s) = \delta_0[1 + \Delta_{se}\cos(\theta_s + \theta_{s0})] \tag{2}$$

where Δ_{se} represents the static eccentricity severity, ranging from 0 to 1. It is defined as the ratio of the eccentricity length to the original airgap length. The angle θ_{s0} is an auxiliary coordinate which allows for adjusting the position of maximum airgap length.

In turn, when dynamic eccentricity is considered, the airgap length can be expressed as a function of both θ_s and the rotor angular position θ_r, as described by the following:

$$\delta(\theta_s, \theta_r) = \delta_0[1 + \Delta_{de}\cos(\theta_s + \theta_r + \theta_{s0})] \tag{3}$$

where Δ_{de} is the dynamic eccentricity severity, also ranging from 0 to 1. In turn, θ_r is a function of rotor speed and time, resulting in a dynamic variation in the airgap.

Lastly, for mixed eccentricity, the airgap length can be described combining (2) and (3) as follows:

$$\delta(\theta_s, \theta_r) = \delta_0[1 + \Delta_{se}\cos(\theta_s + \theta_{s0}) + \Delta_{de}\cos(\theta_s + \theta_r + \theta_{s1})] \quad (4)$$

Implementing eccentricity in an FE model can be challenging if the quality of the mesh and the time step are not properly considered. The present work implements static eccentricity by devising a static translation vector that acts on the stationary parts of the model. The magnitude of this vector is given by $\delta_0\Delta_{se}$. For the dynamic eccentricity, all moving parts of the model are translated dynamically according to a rotating vector of magnitude $\delta_0\Delta_{de}$. Mixed eccentricity takes into account the combination of both translating vectors.

In this paper, and following suggested values in the literature, moderate to severe eccentricity (up to 50% of the airgap length) is evaluated, considering the following conditions:

- **Static eccentricity** with two degrees: $\Delta_{se} = 0.25$ and $\Delta_{de} = 0.5$
- **Dynamic eccentricity** with two degrees: $\Delta_{de} = 0.25$ and $\Delta_{de} = 0.5$
- **Mixed eccentricity** with one degree: $\Delta_{se} = 0.25$ and $\Delta_{de} = 0.25$

3.2.2. Broken Rotor Bars in SCIMs

In this work, the analysis of broken bars is conducted by changing the electrical conductivity of the material associated with each rotor bar in the equivalent circuit of the 2D FE model. Three levels of fault severity are considered, in concordance with related studies for the detection of broken bars in commercial IMs [27,29,62,63]:

- **Level 1:** The electrical conductivity of the first rotor bar is modified to $\sigma_1 = 0.5\sigma_0$, representing an initial broken bar scenario, which is a precursor to full bar breakage.
- **Level 2:** The electrical conductivity of the first rotor bar is modified to $\sigma_1 = 0$, representing an incipient broken bar scenario.
- **Level 3:** The electrical conductivity of the first three rotor bars is modified to $\sigma_1 = \sigma_2 = \sigma_3 = 0$, which represents a severe broken bar scenario.

It should be noted that the analysis is conducted with the assumption of maximum asymmetry in the broken bars, to assess the worst-case scenarios in terms of performance degradation.

3.2.3. Partial Demagnetization in PMSMs

Demagnetization is defined as the irreversible reduction in the remanent magnetic flux density of one or more magnets. It can be classified into two types: uniform irreversible demagnetization (UD) and partial irreversible demagnetization (PD). UD occurs when the remanent flux density of all the magnets in the rotor is reduced by the same ratio, whereas PD occurs when the remanent flux density is reduced in only some of the magnets [64].

Since UD is uncommon in real-world cases, only PD was investigated in the machine specimens. Considering a surface-mounted PMSM, each magnet can be divided into Q_p sectors, and the demagnetization of the i-th pole can be defined as follows:

$$\Delta B_{r,i} = \frac{1}{Q_p}\sum_{j=1}^{Q_p} k_{j,i} \quad (5)$$

where $k_{j,i}$ is a factor that accounts for the demagnetization of the j-th sector of the i-th magnet, ranging from 0 to 1. If a magnet sector is flawless, the value is 0, while if the

magnet sector is completely demagnetized, the value is 1. Considering the above, the total demagnetization of a PMSM can be expressed as follows:

$$\Delta B_{\mathrm{r,total}} = \frac{1}{2pQ_{\mathrm{p}}} \sum_{i=1}^{2p} \sum_{j=1}^{Q_{\mathrm{p}}} k_{j,i} \tag{6}$$

where p is the factor that accounts for the demagnetization of the j-th sector of the i-th magnet ranging.

In this paper, and similarly to related studies on PD [64–66], four levels of PD were analyzed:

- **Level 1:** A 50% demagnetization is applied in half of the magnet of one pole ($\Delta B_{\mathrm{r},1} = 0.25$), representing an initial PD scenario.
- **Level 2:** A 50% demagnetization is applied in the entire magnet of one pole ($\Delta B_{\mathrm{r},1} = 0.5$), representing an incipient PD scenario.
- **Level 3:** A 50% demagnetization is applied in half of the magnet of several adjacent poles to account for an overall ~10% of total demagnetization ($\Delta B_{\mathrm{r,total}} = 0.1$), representing a mild scenario.
- **Level 4:** A 50% demagnetization is applied in half of the magnet of several adjacent poles to account for an overall ~20% of total demagnetization ($\Delta B_{\mathrm{r,total}} = 0.2$), representing a moderate scenario.

3.3. FE Simulation Considerations

The 2D FE simulations were used to evaluate the performance of the selected LSHT machines, utilizing the commercial package ANSYS Electronics Desktop 2024R1 to directly evaluate electromagnetic variables and the commercial package ANSYS Workbench 2024R1 to include multi-objective optimization. A quad-layer mesh in the airgap was considered, along with a dense mesh in the tooth tip and slot areas, as illustrated in the following sections. No periodicity condition was applied in order to account for asymmetric faults, and an outer boundary of zero magnetic potential was considered near the outer diameter, which allows for the establishment of stray flux lines and confines the active solving area. Additionally, materials were assigned based on manufacturing data retrieved from ANSYS databases (Granta Producers Materials Data for Simulation). Electromagnetic efficiency computations in these FE simulations include stator winding losses, stator iron losses, magnet losses (if applicable), rotor solid conductor losses (if applicable), and rotor iron losses. Stator winding losses are calculated from the phase stator current and stator resistance. Stator and rotor iron losses, when laminated, are computed using the coefficients of hysteresis loss, excess loss, direct current loss, and eddy current loss, based on an electrical steel loss model. Solid losses are directly computed by the FE software, and end-winding effects are addressed by including pre-computed end-winding leakage inductance values. In turn, mechanical losses were neglected in order to maintain a focused scope on the electromagnetic performance. In Figure 5, a flowchart of the treatment of FE results is provided.

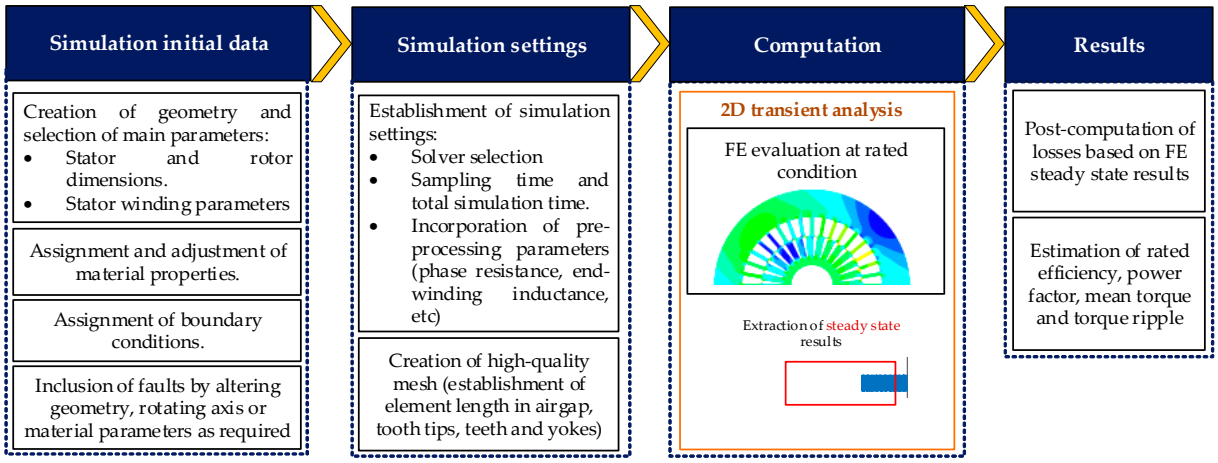


Figure 5. Flowchart of the assessment of selected machines using FE simulations.

4. Results: Design and Evaluation of LSHT Machines

This section presents the results of the design process of 10-pole and 16-pole LSHT IMs, SynRMs, and PMSMs from the multi-objective optimization procedure described in Section 3.1.

4.1. The 10-Pole LSHT Designs Obtained Through Multi-Objective Optimization

The optimization problem previously described in Table 1 was solved for the 10-pole LSHT machines. Figure 6 illustrates the evolution of the optimization process, displaying the mean torque and efficiency of the machine specimens. The geometry of stator and rotor structures of the best 10-pole LSHT machines is shown in Figure 7, while the mesh used for the fault assignments in the 2D FE models is illustrated in Figure 8. The main dimensions and specifications of the machines are presented in Appendix A, Table A1.

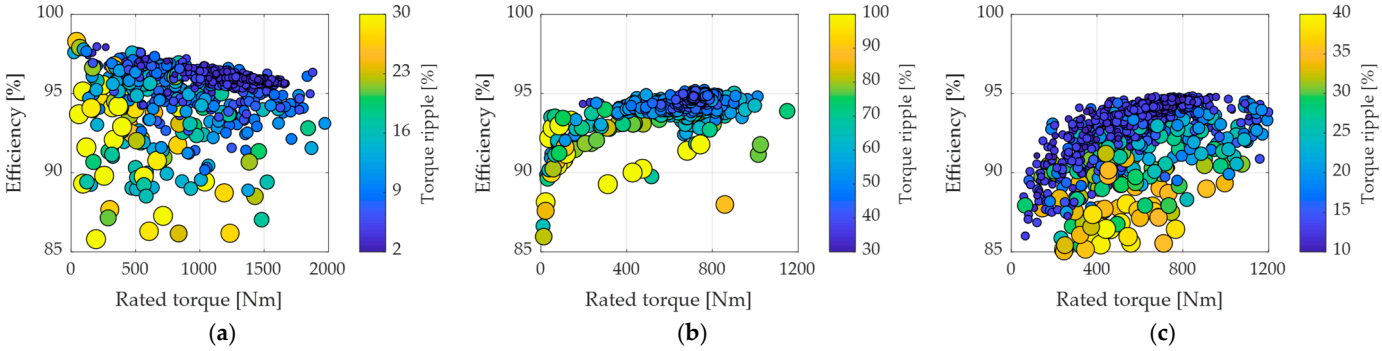
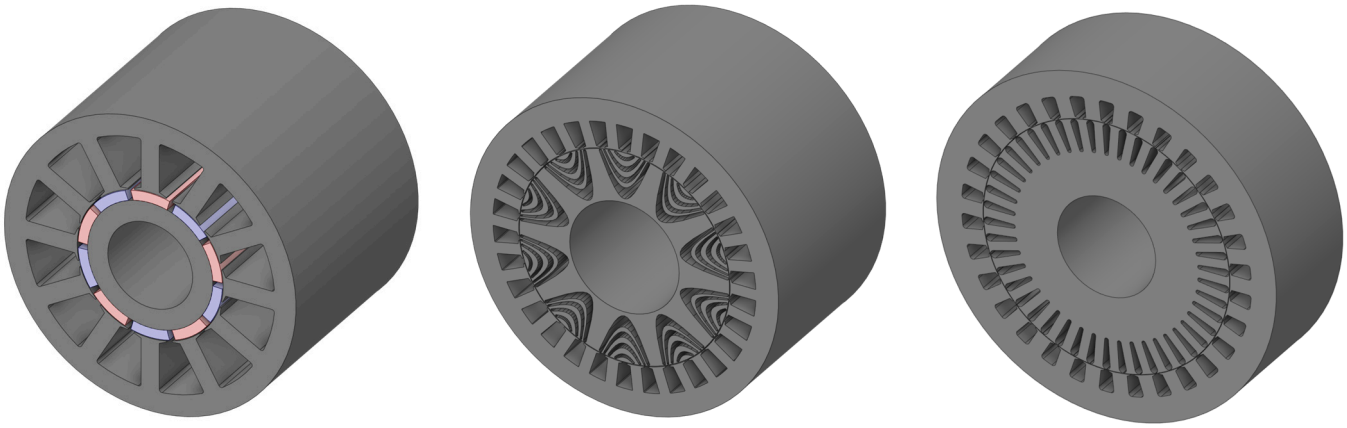


Figure 6. Optimized machines for 10-pole LSHT applications: (**a**) PMSM; (**b**) SynRM; (**c**) SCIM.

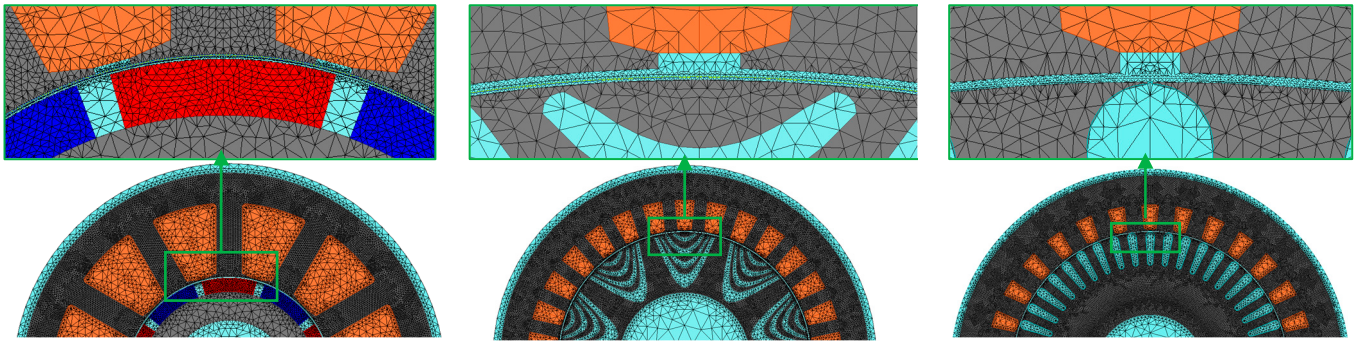
The performance of the best designs obtained from the optimization process is summarized in Table 2, with a focus on rated performance. From the results, it is evident that the PMSM outperforms the SynRM and the IM in terms of torque capacity, efficiency, and power factor, largely due to the adoption of permanent magnets and the superior performance provided by fractional-slot concentrated windings. This is in agreement with most research related to LSHT designs. Nonetheless, among rare-earth-free topologies, the SynRM and IM exhibit comparable torque capacities, with the SynRM having a slight margin over the IM. In turn, the IM offers a notably lower torque ripple and a higher power factor. Although the performance of the SynRM could be improved through step skewing or adopting an asymmetric design, this is outside the scope of this paper, which focuses on fault evaluation [55]. Additionally, the SynRM suffers from a very low power factor, which

can be associated to the saliency effects at high pole counts. It is important to note that neither the PMSM nor the SynRM has self-starting capability.



(a) (b) (c)

Figure 7. The resulting optimized 10-pole LSHT machines in 3D sketches: (**a**) PMSM; (**b**) SynRM; (**c**) SCIM.



(a) (b) (c)

Figure 8. The 2D FE model used for the evaluation of 10-pole LSHT machines: (**a**) meshed best PMSM model; (**b**) meshed best SynRM model; (**c**) meshed best SCIM model. A quad-layer airgap was considered in all FE models to enhance accuracy.

Table 2. Main performance comparison of the optimized 10-pole LSHT machines.

Parameter	Symbol	PMSM	SynRM	SCIM
Mean Torque	T_{mean} [Nm]	1360.9	716.8	700.1
Torque Ripple	T_{rp} [%]	4.50	42.9	3.9
Efficiency	η [%]	97.3	94.4	94.2
Active Losses	$L_{cp+fe+edd}$ [W]	2329	2650	2699
Power Factor	pf [−]	0.98	0.47	0.78

4.2. The 16-Pole LSHT Designs Obtained Through Multi-Objective Optimization

The raw optimization data for the 16-pole machines are presented in Figure 9. The geometry of stator and rotor structures of the best 16-pole LSHT machines is shown in Figure 10, and the mesh considered for the fault assignments in the 2D FE model is illustrated in Figure 11. Further details regarding the dimensions and materials of the machines are provided in Appendix A.

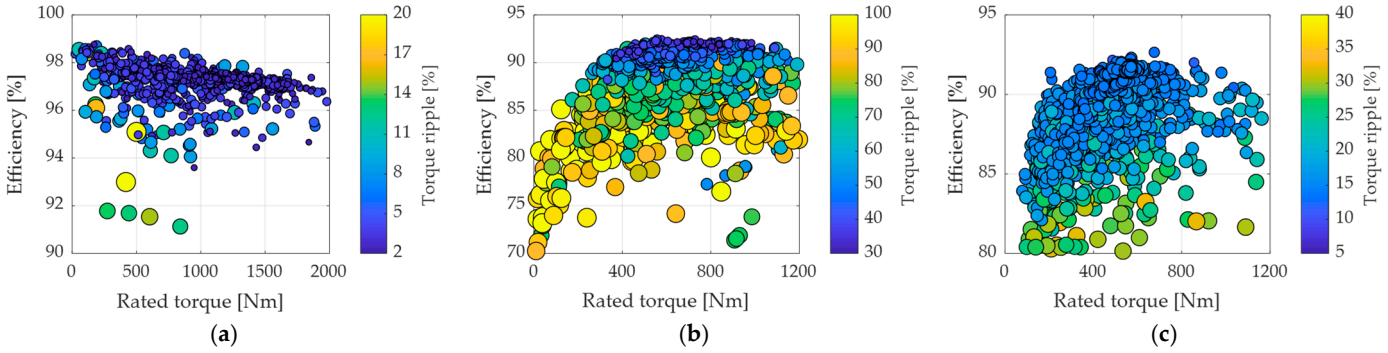


Figure 9. Optimized LSHT 16-pole machines: (**a**) PMSM; (**b**) SynRM; (**c**) SCIM.

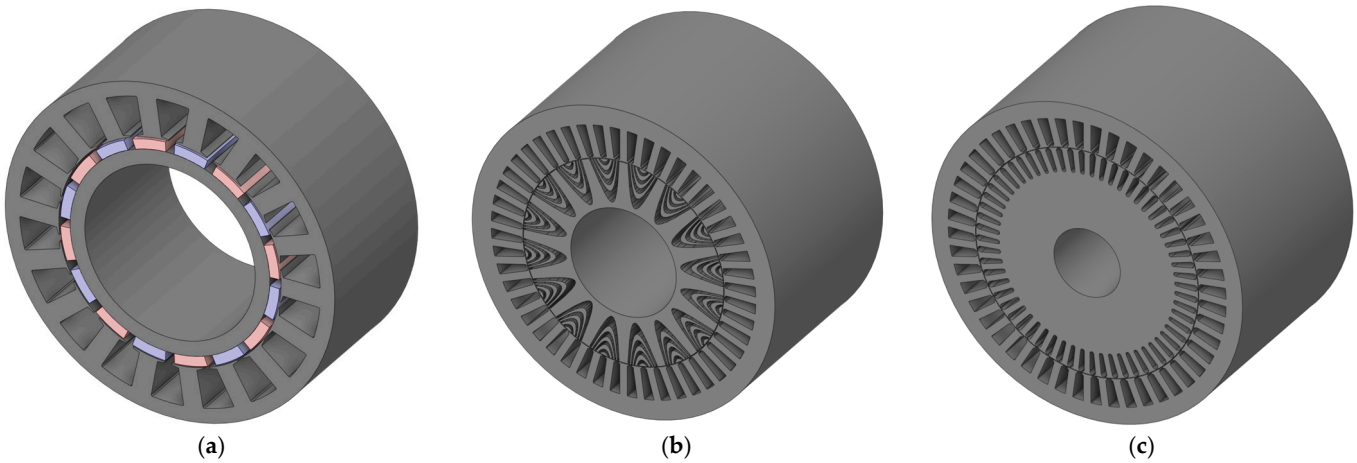


Figure 10. The resulting optimized 16-pole LSHT machines in 3D sketches: (**a**) PMSM; (**b**) SynRM; (**c**) SCIM.

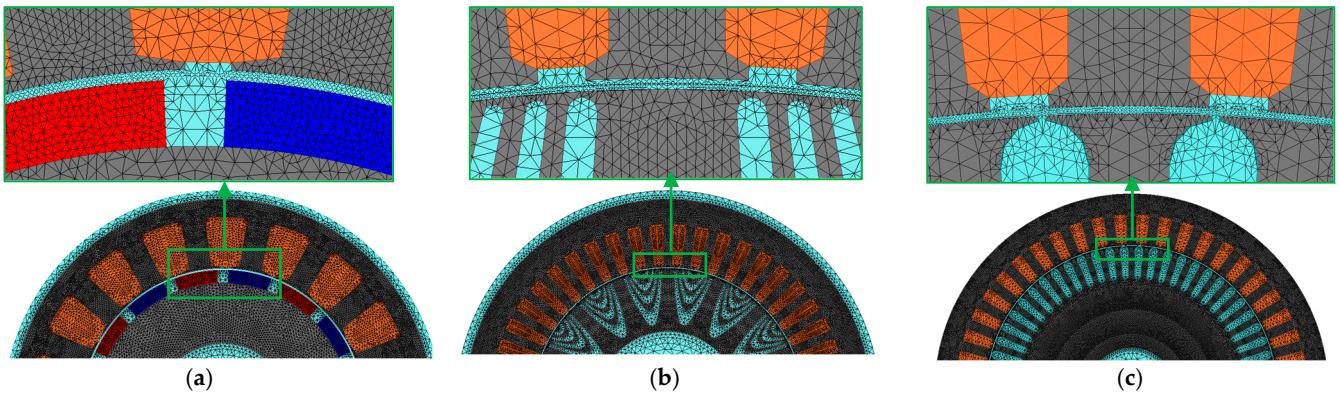


Figure 11. The 2D FE model used for the evaluation of 16-pole LSHT machines: (**a**) meshed best PMSM model; (**b**) meshed best SynRM model; (**c**) meshed best SCIM model. A quad-layer airgap was considered in all FE models to enhance accuracy.

The performance of the best designs obtained after solving this optimization process is summarized in Table 3, focusing on rated performance.

Table 3. Main performance comparison of the optimized 16-pole LSHT machines.

Parameter	Symbol	PMSM	SynRM	SCIM
Mean Torque	T_{mean} [Nm]	1522	608.6	640.1
Torque Ripple	T_{rp} [%]	2.7	45.4	10.8
Efficiency	η [%]	96.3	90.3	90.7
Active Losses	$L_{cp+fe+edd}$ [W]	2258	2565	2543
Power Factor	pf [−]	0.98	0.35	0.63

The evaluation results show that the PMSM continues to be the best performer in terms of torque capacity, efficiency, and power factor, significantly outperforming the SynRM and the IM. In contrast with the results for the 10-pole machines, the 16-pole IM has a slight advantage in torque capacity when compared to the 16-pole SynRM. In addition, the IM significantly surpasses the SynRM in torque ripple, achieving a value below 6%. The SynRM continues to offer relatively high efficiency but suffers from a significantly low power factor. In summary, among rare-earth-free topologies, the IM outperforms the SynRM in torque capacity, torque ripple, and efficiency for the 16-pole configuration.

5. Results: Impact of Faults in LSHT Machines

This section presents the results of evaluating the impact of faults in 10-pole and 16-pole LSHT IMs, SynRMs, and PMSMs, following the guidelines outlined in Section 3.2.

5.1. Evaluation of Shared Faults Across 10-Pole and 16-Pole LSHT Machines

The variation in the performance metrics after the implementation of the different eccentricity types described in Section 3.2.1 is presented in Table 4 for the 10-pole machines. From the results, the following can be noted:

- Static and dynamic eccentricity do not have a significant impact on the torque capacity. The mean torque variability is lower than 0.1% in the PMSM, lower than 0.8% in the SynRM, and lower than 0.8% in the SCIM.
- Static and dynamic eccentricity do not have a significant impact on losses. The variability is lower than 0.2% for the PMSM, lower than 0.5% for the SynRM, and lower than 0.2% for the SCIM.
- Static and dynamic eccentricity have virtually no effect on efficiency or power factor for all machines.
- Static and dynamic eccentricity impact the torque ripple of different topologies in distinct ways. For the PMSM, no significant effects were observed. However, for both the SynRM and the SCIM, a slight increase in the ripple was noted at higher eccentricity values, specifically when $\Delta_{se} + \Delta_{de} = 0.5$.

It can be noted that the effect on torque ripple is relatively mild and may be difficult to detect in systems lacking direct torque measurement capabilities. Additionally, variations in torque ripple can arise from a range of electromagnetic and mechanical factors. Detecting this phenomenon through speed ripple analysis would also be challenging, as it is heavily influenced by the inertia of the system. It can therefore be concluded that static and dynamic eccentricities cannot be directly detected by monitoring basic performance metrics in the 10-pole LSHT PMSM, SynRM, and SCIM.

For the 16-pole machines, the variation in performance metrics after the implementation of the different eccentricity types described in Section 3.2.1 is presented in Table 5.

Table 4. Main performance comparison of optimized 10-pole LSHT machines including eccentricities faults.

	Parameter	Symbol	PMSM	SynRM	SCIM
Healthy	Mean Torque	T_{mean} [Nm]	1360.9	716.8	700.1
	Torque Ripple	T_{rp} [%]	4.5	42.9	3.9
	Efficiency	η [%]	97.3	94.4	94.2
	Active Losses	$L_{cp+fe+edd}$ [W]	2329	2650	2699
	Power Factor	pf [−]	0.98	0.47	0.78
Dynamic $\Delta_{de} = 0.25$	Mean Torque	T_{mean} [Nm]	1361	719.2	700.8
	Torque Ripple	T_{rp} [%]	4.6	44.0	3.5
	Efficiency	η [%]	97.3	94.4	94.2
	Active Losses	$L_{cp+fe+edd}$ [W]	2323	2661	2695
	Power Factor	pf [−]	0.98	0.47	0.78
Dynamic $\Delta_{de} = 0.5$	Mean Torque	T_{mean} [Nm]	1361.0	717.9	700.5
	Torque Ripple	T_{rp} [%]	4.6	44.2	5.4
	Efficiency	η [%]	97.3	94.4	94.2
	Active Losses	$L_{cp+fe+edd}$ [W]	2323	2650	2695
	Power Factor	pf [−]	0.98	0.47	0.78
Static $\Delta_{se} = 0.25$	Mean Torque	T_{mean} [Nm]	1360.9	713.7	703.5
	Torque Ripple	T_{rp} [%]	4.6	44.5	3.47
	Efficiency	η [%]	97.3	94.4	94.2
	Active Losses	$L_{cp+fe+edd}$ [W]	2323	2664	2696
	Power Factor	pf [−]	0.98	0.47	0.78
Static $\Delta_{se} = 0.5$	Mean Torque	T_{mean} [Nm]	1360.5	714.4	704.1
	Torque Ripple	T_{rp} [%]	4.7	45.0	4.8
	Efficiency	η [%]	97.3	94.4	94.2
	Active Losses	$L_{cp+fe+edd}$ [W]	2327	2661	2698
	Power Factor	pf [−]	0.98	0.47	0.78
Dynamic & Static $\Delta_{se} = 0.25$ and $\Delta_{de} = 0.25$	Mean Torque	T_{mean} [Nm]	1361.1	717.8	700.9
	Torque Ripple	T_{rp} [%]	4.8	44.0	5.0
	Efficiency	η [%]	97.3	94.4	94.2
	Active Losses	$L_{cp+fe+edd}$ [W]	2323	2667	2694
	Power Factor	pf [−]	0.98	0.47	0.78

From the evaluation, the following can be stated:

- Static and dynamic eccentricities do not have a significant effect on the mean torque. The variability is lower than 0.5% across the PMSM, SynRM, and SCIM.
- Static and dynamic eccentricity do not have a significant impact on losses. The variability is lower than 0.7% for the PMSM, the SynRM, and the SCIM.
- Static and dynamic eccentricity have virtually no effect on efficiency or power factor for all machines.
- Static and dynamic eccentricity affect the torque ripple differently across the different topologies. For the PMSM, a 45% increase in the ripple was observed with static and dynamic eccentricity values of $\Delta_{se} = 0.5$ and $\Delta_{de} = 0.5$, while a 12% increase occurred for lower eccentricity severities ($\Delta_{se} = 0.25$ and $\Delta_{de} = 0.25$). In the case of the SynRM, ripple variations remained below 10% across all severity scenarios, with minimal impact from low-severity eccentricities ($\Delta_{se} = 0.25$ and $\Delta_{de} = 0.25$). The SCIM displayed a similar trend to the SynRM, with ripple variations below 12% for the most severe cases, and under 3% for lower eccentricity values.

Table 5. Main performance data comparison of optimized 16-pole LSHT machines including eccentricities faults.

	Parameter	Symbol	PMSM	SynRM	SCIM
Healthy	Mean Torque	T_{mean} [Nm]	1522	607.7	640.1
	Torque Ripple	T_{rp} [%]	2.7	45.4	10.8
	Efficiency	η [%]	96.2	90.3	90.7
	Active Losses	$L_{cp+fe+edd}$ [W]	2358	2565	2543
	Power Factor	pf [−]	0.98	0.36	0.63
Dynamic $\Delta_{de} = 0.25$	Mean Torque	T_{mean} [Nm]	1523	608.7	641.7
	Torque Ripple	T_{rp} [%]	3.0	46.3	11.1
	Efficiency	η [%]	96.2	90.3	90.7
	Active Losses	$L_{cp+fe+edd}$ [W]	2363	2568	2544
	Power Factor	pf [−]	0.98	0.36	0.63
Dynamic $\Delta_{de} = 0.5$	Mean Torque	T_{mean} [Nm]	1524	612.7	649.2
	Torque Ripple	T_{rp} [%]	4.1	49.8	12.2
	Efficiency	η [%]	96.2	90.3	90.7
	Active Losses	$L_{cp+fe+edd}$ [W]	2373	2581	2560
	Power Factor	pf [−]	0.98	0.36	0.63
Static $\Delta_{se} = 0.25$	Mean Torque	T_{mean} [Nm]	1522	606.6	639.5
	Torque Ripple	T_{rp} [%]	3.0	44.5	10.6
	Efficiency	η [%]	96.2	90.3	90.7
	Active Losses	$L_{cp+fe+edd}$ [W]	2361	2566	2552
	Power Factor	pf [−]	0.98	0.36	0.63
Static $\Delta_{se} = 0.5$	Mean Torque	T_{mean} [Nm]	1523	611.0	642.3
	Torque Ripple	T_{rp} [%]	3.9	47.7	11.6
	Efficiency	η [%]	96.2	90.3	90.7
	Active Losses	$L_{cp+fe+edd}$ [W]	2371	2579	2552
	Power Factor	pf [−]	0.98	0.36	0.63
Dynamic & Static $\Delta_{se} = 0.25$ and $\Delta_{de} = 0.25$	Mean Torque	T_{mean} [Nm]	1523	607.8	642.3
	Torque Ripple	T_{rp} [%]	4.3	46.0	12.1
	Efficiency	η [%]	96.2	90.3	90.7
	Active Losses	$L_{cp+fe+edd}$ [W]	2361	2553	2542
	Power Factor	pf [−]	0.98	0.36	0.63

Compared to the 10-pole machines, the most significant effect on the torque ripple is observed in the 16-pole PMSM. A significant torque ripple increase was obtained, which can be explained from the alteration of rotor symmetry, leading to higher cogging torque that contributes to the ripple waveform. Nevertheless, torque ripple variations are influenced by multiple factors and cannot be directly linked to eccentricity, making it difficult to predict eccentricity from ripple observation alone. It can be concluded that SE and DE cannot be directly detected from monitoring the basic performance metrics in the 16-pole LSHT PMSM, SynRM, and SCIM.

5.2. Evaluation of Faults Specific to SCIMs: Broken Rotor Bars

The variation in performance metrics following the different broken bar levels described in Section 3.2.2 is presented in Table 6 for the 10-pole IM. From the results, it can be noted that the presence of broken bars has minimal impact on torque capacity, efficiency, losses, or power factor. However, in the severe case evaluated, i.e., when three rotor bars are broken, a slight reduction in torque and power factor is observed.

Table 6. Main performance data comparison of optimized 10-pole SCIM LSHT machines including broken bars.

Parameter	Symbol	Healthy	Level 1	Level 2	Level 3
Mean Torque	T_{mean} [Nm]	700.1	700.5	700.0	684
Torque Ripple	T_{rp} [%]	3.9	6.4	10.5	20.5
Efficiency	η [%]	94.2	94.1	94.1	94.0
Active Losses	$L_{cp+fe+edd}$ [W]	2699	2703	2708	2719
Power Factor	pf [−]	0.78	0.78	0.77	0.73

The most notable effect of broken bars is observed in the torque ripple, which increases progressively as more bars fail. Specifically, the torque ripple increases by 64%, 169%, and 426% at severity levels 1, 2, and 3, respectively.

Table 7 summarizes the variation in the performance metrics after the implementation of the different broken bar severities described in Section 3.2.2 for the 16-pole IM.

Table 7. Main performance data comparison of optimized 16-pole SCIM LSHT machines including broken bars.

Parameter	Symbol	Healthy	Level 1	Level 2	Level 3
Mean Torque	T_{mean} [Nm]	640.1	639.5	636.0	629.6
Torque Ripple	T_{rp} [%]	10.8	12.5	15.4	24.2
Efficiency	η [%]	90.7	90.7	90.6	90.5
Active Losses	$L_{cp+fe+edd}$ [W]	2543	2545	2550	2558
Power Factor	pf [−]	0.63	0.63	0.62	0.60

Results in Table 7 indicate that the presence of broken bars has a negligible effect on the mean torque, efficiency, losses, or power factor of the 16-pole machine. In contrast with the 10-pole machine, the most severe case evaluated did not have a significant effect on torque capacity for the 16-pole machine, likely due to the increased number of rotor bars.

The most notable effect of broken bars, similar to that observed for the 10-pole machine, is seen in the torque ripple, which increases progressively as more broken bars are considered. In this 16-pole IM, the torque ripple increases by 16%, 43%, and 124% at severity levels 1, 2, and 3, respectively.

Furthermore, it was observed from a torque waveform inspection that the dominant torque ripple harmonics, in the presence of broken bars, are related to the slip value and result from rotor asymmetry. This differs from the well-known 60-electrical-degree period associated with torque ripple in three-phase machines. For the 10-pole machine, the main frequency of the torque ripple is 1.25 Hz, while for the 16-pole machine, it is 1.5 Hz. The slip values for these machines are 1.23% and 1.5%, respectively.

5.3. Evaluation of Faults Specific to PMSMs: Partial Demagnetization

Table 8 shows the variation in the performance metrics of the 10-pole LSHT machines after applying the different levels of demagnetization, as outlined of Section 3.2.3.

The results for the 10-pole machine indicate that demagnetization levels 1 and 2 have a low impact on the performance of the PMSM, with torque reductions below 5%. Specifically for level 2, where $\Delta B_{r,total} = 5\%$, the torque reduction is directly associated with this change in remanence. At level 3, with $\Delta B_{r,total} = 10\%$, the mean torque is reduced by 8.6% and losses decrease by 3.2%. This reduction in losses can be attributed to the lower magnet

remanence, which leads to a decrease in magnet losses and a reduction in iron losses. Iron losses are influenced by both frequency and flux density as established by [67]:

$$dP_{\text{iron}} = k_{\text{h}} f B_{\text{m}}^2 + \frac{\sigma d_{\text{l}}^2}{12}\left(\frac{dB(t)}{dt}\right)^2 + k_{\text{e}}\left(\frac{dB(t)}{dt}\right)^{1.5} \quad (7)$$

where $B(t)$ is the flux density in the iron core, B_{m} is the amplitude of $B(t)$, f is the electrical frequency, σ is the iron conductivity, d_{l} is the lamination thickness, and k_{h} and k_{e} correspond to coefficients of hysteresis loss and excess loss, respectively. When a group of magnets has a reduced remanence, then there are regions of the stator core that will have a lower flux density magnitude, hence reducing B_{m} and dB/dt, which translates into lower losses as per (7). Frequency is not altered by partial demagnetization. As a result, although torque can be significantly reduced, efficiency remains largely unaffected.

Table 8. Main performance data comparison of optimized 10-pole PMSM LSHT machines including partial demagnetization.

Parameter	Symbol	Healthy	Level 1	Level 2	Level 3	Level 4
Mean Torque	T_{mean} [Nm]	1360.9	1346.5	1298.6	1244.4	1132.7
Torque Ripple	T_{rp} [%]	4.5	6.55	8.85	13.31	9.36
Efficiency	η [%]	97.3	97.3	97.3	97.3	97.1
Active Losses	$L_{\text{cp+fe+edd}}$ [W]	2320	2315	2283	2247	2173
Power Factor	pf [−]	0.98	0.98	0.98	0.98	0.98

If the torque needs to be restored to its original rated value, a logical operating point at a rated load, the increased losses will exceed the rated levels, intensifying the thermal stress on the motor and amplifying the demagnetization effect. The same trend observed for level 3 is obtained for level 4, where a 20% total demagnetization leads to a 16.7% reduction in torque capacity and a 6.3% decrease in losses. Furthermore, a relatively linear relationship is observed between the total demagnetization $\Delta B_{\text{r,total}}$ and the reduction in torque capacity.

Another trend observed is the variation in torque ripple across different demagnetization levels. Significant changes are noted, with level 3 showing the most pronounced effect. This is due to the high symmetry and periodicity of the faulty machine associated with this level, which significantly influences cogging torque. In contrast, Level 4, although exhibiting a higher degree of demagnetization, has reduced symmetry and periodicity, resulting in a lesser impact on the machine's cogging torque, hence not contributing to additional ripple variations.

The variation in the performance metrics of the 16-pole LSHT machines is summarized in Table 9.

Table 9. Main performance data comparison of optimized 16-pole PMSM LSHT machines including partial demagnetization.

Parameter	Symbol	Healthy	Level 1	Level 2	Level 3	Level 4
Mean Torque	T_{mean} [Nm]	1522	1515	1479	1396	1254
Torque Ripple	T_{rp} [%]	2.7	4.2	7.0	14.3	10.6
Efficiency	η [%]	96.2	96.2	96.1	96.0	95.8
Active Losses	$L_{\text{cp+fe+edd}}$ [W]	2358	2355	2338	2282	2175
Power Factor	pf [−]	0.98	0.98	0.98	0.98	0.98

Similar trends to those observed for the 10-pole machines are observed for the 16-pole machines. Demagnetization levels 1 and 2 have a mild effect on torque capacity, whereas a

significant impact is observed for levels 3 and 4. When $\Delta B_{r,total} = 10\%$, torque reduction is 8.3%, and when $\Delta B_{r,total} = 20\%$, torque reduction is 17.6%. In turn, the reduction in losses is 3.2% and 7.7% respectively, the decrease in losses being always lower than the torque reduction. Trends for torque ripple are similar to those of the 10-pole machines. It is important to note that, regardless of the demagnetization level and pole count, the decrease in losses is always lower than the torque reduction. This means that restoring the torque to match the rated load would lead to higher thermal stress.

6. Conclusions

This paper described and quantified the impact of rotor faults on the performance of LSHT machines. Specifically, 10-pole and 16-pole SynRMs, PMSMs, and SCIMs were assessed by means of detailed 2D FE simulations.

Results of the evaluation for each topology can be summarized in Table 10, focusing on the severity of the impact of each fault on the relevant performance metrics.

Table 10. Summary of the impact of common faults on the evaluated LSHT machines.

	Eccentricity on PMSM	Eccentricity on SynRM	Eccentricity on SCIM	Demagnetization on PMSM	Broken Rotor Bars on SCIM
Mean Torque	No effect	No effect	No effect	Moderate impact	Low impact
Torque Ripple	Moderate impact	Low impact	Low impact	High impact	High impact
Efficiency	No effect	No effect	No effect	No effect	No effect
Active Losses	No effect	No effect	No effect	Moderate impact	Low impact
Power Factor	No effect	No effect	No effect	No effect	No effect

The results indicate that performance of the SynRM is relatively unaffected by the analyzed faults. This behavior underlines the necessity of using specific diagnostic techniques to detect eccentricity and misalignments, which are commonly present in this topology.

Additionally, it should be noted that torque ripple is affected by all the evaluated faults. This may suggest that torque ripple is not useful or practical in industrial settings for fault diagnosis, as its behavior is affected by each fault type, specific equipment is required for measuring it, and machine intervention is required. Furthermore, obtaining variations in torque ripple from speed ripple is inconsistent due to factors such as inertia, mechanical transfer functions, and other dynamic phenomena. Nevertheless, it was found that each fault affects torque ripple differently, generating unique torque waveform alterations. This presents an interesting area for future analysis in LSHT machines.

The results also indicate that some faults trigger a reduction in torque capacity, which does not necessarily correlate with the machine producing less torque in a motor-load system. Since torque is determined by the load, a reduction in torque capacity translates into a higher current draw and increased losses, which amplify the thermal stress on the machine.

From the above discussion, it can be concluded that common faults in LSHT machines cannot be directly or easily detected by measuring basic performance metrics. Future research could focus on a more in-depth analysis of torque ripple variations in the presence of typical faults.

Author Contributions: Conceptualization, C.M.-C. and J.E.R.-S.; methodology, C.M.-C. and C.G.; software, C.M.-C. and C.G.; validation, J.E.R.-S. and J.A.A.-D.; formal analysis, C.M.-C.; investigation, C.M.-C. and C.G.; resources, J.A.A.-D. and J.A.T.; data curation, C.M.-C. and C.G.; writing—original draft preparation, C.M.-C., C.G. and J.E.R.-S.; writing—review and editing, J.A.T. and J.A.A.-D.; visualization, C.M.-C.; supervision, J.A.T. and J.A.A.-D.; project administration, J.A.A.-D. and C.M.-C.;

funding acquisition, J.A.A.-D., J.A.T. and C.M.-C. All authors have read and agreed to the published version of the manuscript.

Funding: This research was funded in part by AGENCIA NACIONAL DE INVESTIGACION Y DESARROLLO, grants number FONDECYT1230670 and VIU24P0127, and in part by the Spanish 'Ministerio de Ciencia e Innovación', Agencia Estatal de Investigación and FEDER program in the framework of the "Proyectos de Generación del Conocimiento 2021" of the "Programa Estatal para Impulsar Investigación Científico-Técnica y en su Transferencia," belonging to the "Plan Estatal de Investigación Científica, Técnica e Innovación 2021-2023" under Grant PID2021-122343OB-I00.

Institutional Review Board Statement: Not applicable.

Informed Consent Statement: Not applicable.

Data Availability Statement: The original contributions presented in the study are included in the article, further inquiries can be directed to the corresponding author.

Conflicts of Interest: The authors declare no conflicts of interest.

Appendix A

Table A1. Main data of the optimized 10-pole LSHT machines.

Parameter	Symbol	PMSM	SynRM	SCIM
Stator Outer Diameter	D_{os} [mm]	448.7	475.6	571.5
Stator Inner Diameter	D_{is} [mm]	224.9	326.5	408.4
Stator Slot Height	h_s [mm]	76.2	37.1	34.5
Stator Tooth Width	w_s [mm]	27.9	17.0	25.4
Stator Slot Number	Q_s [−]	12	30	30
Stator Turns per coil	N_s [−]	15	5	5
Airgap length	g [mm]	1.5	1.2	1.0
Rotor Inner Diameter	D_{or} [mm]	130.6	169.0	162.5
PM height	h_{PM} [mm]	14.7	-	-
PM span	α [−]	0.86	-	-
PM segments	−	5	-	-
Stack length	l_{stk} [mm]	325.8	286.6	194.5
Barrier Number	−	-	4	-
Insulation Ratio	k_{air} [−]	-	0.52	-
Rotor Slot Height	h_r [mm]	-	-	49.2
Rotor Tooth Width	w_r [mm]	-	-	13.7
Rotor Slot Number	Q_r [−]	-	-	46

Table A2. Main data of the optimized 16-pole LSHT machines.

Parameter	Symbol	PMSM	SynRM	SCIM
Stator Outer Diameter	D_{os} [mm]	499.8	470.7	551.9
Stator Inner Diameter	D_{is} [mm]	337.2	313.2	407.5
Stator Slot Height	h_s [mm]	56.6	46.5	38.6
Stator Tooth Width	w_s [mm]	21.8	11.3	14.9
Stator Slot Number	Q_s [−]	18	48	48
Stator Turns per coil	N_s [−]	20	5	5
Airgap length	g [mm]	2.4	1.1	1.0
Rotor Inner Diameter	D_{or} [mm]	258.6	164.1	121.5
PM height	h_{PM} [mm]	14.7	-	-
PM span	α [−]	0.78	-	-
PM segments	−	5	-	-

Table A2. *Cont.*

Parameter	Symbol	PMSM	SynRM	SCIM
Stack length	l_{stk} [mm]	218.2	290.5	209.9
Barrier Number	–	-	4	-
Insulation Ratio	k_{air} [−]	-	0.49	-
Rotor Slot Height	h_r [mm]	-	-	45.0
Rotor Tooth Width	w_r [mm]	-	-	9.9
Rotor Slot Number	Q_r [−]	-	-	60

Table A3. Materials used in the active part of the machines.

Active Part	Machines	Material
Stator Lamination	SCIM, PMSM and SynRM	Non-Oriented Silicon Steel (M350-50A)
Rotor Lamination	SCIM, PMSM and SynRM	Non-Oriented Silicon Steel (M350-50A)
Stator coils	SCIM, PMSM and SynRM	Copper
Rotor bars	SCIM	Aluminum
Magnets	PMSM	NdFeB

References

1. Antonino-Daviu, J.A.; Zamudio-Ramirez, I.; Osornio-Rios, R.A.; Dunai, L. Fault Diagnosis in Electric Motors through the Analysis of Currents and Stray Fluxes. In Proceedings of the 2023 International Conference on Electromechanical and Energy Systems (SIELMEN), Craiova, Romania, 11–13 October 2023; pp. 1–7.
2. Gundewar, S.K.; Kane, P.V. Condition Monitoring and Fault Diagnosis of Induction Motor. *J. Vib. Eng. Technol.* **2021**, *9*, 643–674. [CrossRef]
3. Liu, Z.; Zhang, P.; He, S.; Huang, J. A Review of Modeling and Diagnostic Techniques for Eccentricity Fault in Electric Machines. *Energies* **2021**, *14*, 4296. [CrossRef]
4. Choi, S.; Haque, M.S.; Tarek, M.T.B.; Mulpuri, V.; Duan, Y.; Das, S.; Garg, V.; Ionel, D.M.; Masrur, M.A.; Mirafzal, B.; et al. Fault diagnosis techniques for permanent magnet ac machine and drives—A review of current state of the art. *IEEE Trans. Transp. Electrif.* **2018**, *4*, 444–463. [CrossRef]
5. Allianz Insurance. *Monitoring und Diagnose Elektrischer Maschinen und Antriebe*; VDE Colloquium: Munich, Germany, 28 June 2001.
6. Al-Badri, M.; Pillay, P. Modified Efficiency Estimation Tool for Three-Phase Induction Motors. *IEEE Trans. Energy Convers.* **2023**, *38*, 771–779. [CrossRef]
7. Lee, S.B.; Stone, G.C.; Antonino-Daviu, J.; Gyftakis, K.N.; Strangas, E.G.; Maussion, P.; Platero, C.A. Condition Monitoring of Industrial Electric Machines: State of the Art and Future Challenges. *IEEE Ind. Electron. Mag.* **2020**, *14*, 158–167. [CrossRef]
8. Faiz, J.; Joksimovic, G.; Ghorbanian, V. *Fault Diagnosis of Induction Motors*; Institution of Engineering & Technology: Stevenage, UK, 2017; 536p. [CrossRef]
9. Hormaz, A.; Ketan, B. An Overview of Techniques for Detecting Mechanical Anomalies in Induction Motors. *Trans. Indian Natl. Acad. Eng.* **2024**, *9*, 71–86. [CrossRef]
10. Anurag, C.; Deepam, G.; Letha, S.S.; Aparna, A. Condition Monitoring and Fault Diagnosis of Induction Motors: A Review. *Arch. Comput. Methods Eng.* **2019**, *26*, 1221–1238. [CrossRef]
11. Moin, S.K.; Sahay, K.; Giri, V.K. Health Monitoring and Fault Diagnosis in Induction Motor-A Review. *Int. J. Adv. Res. Electr. Electron. Instrum. Eng.* **2014**, *3*, 6549–6565.
12. Liang, X.; Ali, M.Z.; Zhang, H. Induction Motors Fault Diagnosis Using Finite Element Method: A Review. *IEEE Trans. Ind. Appl.* **2020**, *56*, 1205–1217. [CrossRef]
13. Li, X.; Tian, X.; Wang, Y.; Zhao, R.; He, W. Analysis of Vibration and Noise of IPMSM for Electric Vehicles under Inverter Harmonic in a Wide-speed Range. In Proceedings of the 2019 22nd International Conference on Electrical Machines and Systems (ICEMS), Harbin, China, 11–14 August 2019; pp. 1–6. [CrossRef]
14. Onsal, M.; Cumhur, B.; Demir, Y.; Yolacan, E.; Aydin, M. Rotor Design Optimization of a New Flux-Assisted Consequent Pole Spoke-Type Permanent Magnet Torque Motor for Low-Speed Applications. *IEEE Trans. Magn.* **2018**, *54*, 1–5. [CrossRef]

15. Wu, D.; Xu, J.; Han, Z.; Lin, H.; Shao, P. Research on Proper Fractional-Slot Concentrated Winding Characteristics for A High Thrust Force Ultra-Low Speed Tubular PM Linear Machine. In Proceedings of the 2023 IEEE International Conference on Applied Superconductivity and Electromagnetic Devices (ASEMD), Tianjin, China, 27–29 October 2023; pp. 1–2.
16. Zhang, Z.; Yu, S.; Zhang, F.; Jin, S.; Wang, X. Electromagnetic and Structural Design of a Novel Low-Speed High-Torque Motor With Dual-Stator and PM-Reluctance Rotor. *IEEE Trans. Appl. Superconduct.* **2020**, *30*, 1–5. [CrossRef]
17. Madariaga, C.; Gallardo, C.; Tapia, N.R.J.A.; Jara, W.; Degano, M. Design and Evaluation of Matrix Rotor Induction Motor for High-Torque Low-Speed Applications. *IEEE Trans. Energy Convers.* 2024; *early access*. [CrossRef]
18. Liang, B.X.; Wang, D.Z.; Zhang, B.Y.; Xu, G.R. Research of Low-Power Low-Speed Squirrel-cage Motor. In Proceedings of the 2019 Chinese Control and Decision Conference (CCDC), Nanchang, China, 3–5 June 2019; pp. 3718–3723.
19. Khaliq, S.; Modarres, M.; Lipo, T.A.; Kwon, B.-I. Design of Novel Axial-Flux Dual Stator Doubly Fed Reluctance Machine. *IEEE Trans. Magn.* **2015**, *51*, 1–4. [CrossRef]
20. Lee, S.G.; Kim, K.-S.; Lee, J.; Kim, W.H. A Novel Methodology for the Demagnetization Analysis of Surface Permanent Magnet Synchronous Motors. *IEEE Trans. Magn.* **2016**, *52*, 1–4. [CrossRef]
21. Baranski, M.; Szelag, W.; Lyskawinski, W. Experimental and Simulation Studies of Partial Demagnetization Process of Permanent Magnets in Electric Motors. *IEEE Trans. Energy Convers.* **2021**, *36*, 3137–3145. [CrossRef]
22. Li, Q.; Ma, C.; Wang, P.; Zhang, X. Analytical Model for IPMSMs with Mixed Eccentricity Considering the Effect of Eccentricity on Core Saturation. *IEEE Trans. Transp. Electrif.* 2024; *early access*. [CrossRef]
23. Ilamparithi, T.C.; Nandi, S. Detection of Eccentricity Faults in Three-Phase Reluctance Synchronous Motor. *IEEE Trans. Ind. Appl.* **2012**, *48*, 1307–1317. [CrossRef]
24. Mahmoud, H.; Bianchi, N. Eccentricity in Synchronous Reluctance Motors—Part I: Analytical and Finite-Element Models. *IEEE Trans. Energy Convers.* **2015**, *30*, 745–753. [CrossRef]
25. Mukherjee, V.; Rasilo, P.; Martin, F.; Belahcen, A. Effect of Magnetic Forces and Magnetostriction on the Stator Vibrations of a Bearingless Synchronous Reluctance Motor. *IEEE Trans. Magn.* **2019**, *55*, 1–4. [CrossRef]
26. Imeryuz, M.; Mergen, A.F.; Ustun, O. A method to analyze asynchronous machines with broken rotor bars. In Proceedings of the SPEEDAM 2010, Pisa, Italy, 14–16 June 2010; pp. 269–272.
27. Sittisrijan, N.; Ruangsinchaiwanich, S. Investigation of the broken bar effect on the squirrel cage induction motor by FEM. In Proceedings of the 2010 International Conference on Electrical Machines and Systems, Incheon, Republic of Korea, 10–13 October 2010; pp. 1297–1302.
28. Muteba, M. Analysis of a Three-Phase Induction Motor with a Double–Triple-Layer Stator Winding Configuration Operating with Broken Rotor Bar Faults. *Machines* **2023**, *11*, 1023. [CrossRef]
29. Fireteanu, V.; Constantin, A.I.; Popa, M. Influence of Single or Multiple Faults Short-circuit, Broken Rotor Bar and Eccentricity on the Torque and Rotor Force in Induction Motors. In Proceedings of the 2018 XIII International Conference on Electrical Machines (ICEM), Alexandroupoli, Greece, 3–6 September 2018; pp. 1868–1874.
30. Kedjar, B.; Merkhouf, A.; Al-Haddad, K. Large Synchronous Machines Diagnosis Based on Air-Gap and Stray Fluxes—An Overview. In Proceedings of the 2020 International Conference on Electrical Machines (ICEM), Gothenburg, Sweden, 23–26 August 2020; pp. 1384–1389.
31. Bernier, S.; Merkhouf, A.; Al-Haddad, K. Diagnosis of Multiple Defects Within Large Hydroelectric Generator Using Stray Flux and Air Gap (Distance and Flux) Measurements. *IEEE Trans. Ind. Appl.* **2024**, *60*, 8687–8700. [CrossRef]
32. Bechara, H.; Ibrahim, R.; Zemouri, R.; Kedjar, B.; Merkhouf, A.; Tahan, A.; Al-Haddad, K. Review of Artificial Intelligence Methods for Faults Monitoring, Diagnosis, and Prognosis in Hydroelectric Synchronous Generators. *IEEE Access* **2024**, *12*, 173599–173617. [CrossRef]
33. Zhou, J.; Fang, H.; Li, R.; Qu, R.; Li, D. Research on Sensitivity of Slot-Pole Combination to Unbalanced Electromagnetic Force Introduced by Rotor Eccentricity. In Proceedings of the 2022 International Conference on Electrical Machines (ICEM), Valencia, Spain, 5–8 September 2022; pp. 2228–2233.
34. Mirimani, S.M.; Vahedi, A.; Marignetti, F. Effect of Inclined Static Eccentricity Fault in Single Stator-Single Rotor Axial Flux Permanent Magnet Machines. *IEEE Trans. Magn.* **2012**, *48*, 143–149. [CrossRef]
35. Guo, B.; Du, Y.; Peng, F.; Huang, Y. Magnetic Field Calculation in Axial Flux Permanent Magnet Motor with Rotor Eccentricity. *IEEE Trans. Magn.* **2022**, *58*, 1–4. [CrossRef]
36. Riquelme, D.; Madariaga, C.; Jara, W.; Bramerdorfer, G.; Tapia, J.A.; Riedemann, J. Study on Stator-Rotor Misalignment in Modular Permanent Magnet Synchronous Machines with Different Slot/Pole Combinations. *Appl. Sci.* **2023**, *13*, 2777. [CrossRef]
37. Jeyasankar, E.; Ahsanullah, K.; Zhenzhen, X.; Panda, S.K. Local demagnetization fault diagnosis for Surface Permanent Magnet based marine propulsion motor. In Proceedings of the 2017 IEEE 3rd International Future Energy Electronics Conference and ECCE Asia (IFEEC 2017—ECCE Asia), Kaohsiung, Taiwan, 4–7 June 2017; pp. 975–979. [CrossRef]
38. Frosini, L. Novel diagnostic techniques for rotating electrical machines—A review. *Energies* **2020**, *13*, 5066. [CrossRef]
39. McMillan, R.B. *Rotating Machinery: Practical Solutions to Unbalance and Misalignment*; River Publishers: Gistrup, Denmark, 2020.

40. Goktas, T.; Arkan, M.; Gurusamy, V. A comparative study of current, vibration and stray magnetic flux based detection for parallel misalignment fault in induction motors. In Proceedings of the 2021 IEEE 13th International Symposium on Diagnostics for Electrical Machines, Power Electronics and Drives (SDEMPED), Dallas, TX, USA, 22–25 August 2021; IEEE: Piscataway, NJ, USA, 2021; Volume 1, pp. 11–16.
41. Corne, B.; Knockaert, J.; Desmet, J. Misalignment and unbalance fault severity estimation using stator current measurements. In Proceedings of the 2017 IEEE 11th International Symposium on Diagnostics for Electrical Machines, Power Electronics and Drives (SDEMPED), Tinos, Greece, 29 August–1 September 2017; IEEE: Piscataway, NJ, USA, 2017; pp. 247–253.
42. Artetxe, G.; Caballero, D.; Prieto, B.; Martinez-Iturralde, M.; Elosegui, I. Eliminating rare earth permanent magnets on low-speed high-torque machines: A performance and cost comparison of synchronous reluctance machines, ferrite permanent magnet-synchronous reluctance machines and permanent magnet synchronous machines for a direct-drive elevator system. *IET Electr. Power Appl.* **2021**, *15*, 370–3378.
43. Kou, S.; Kou, Z.; Wu, J.; Wang, Y. Modeling and simulation of a novel low-speed high-torque permanent magnet synchronous motor with asymmetric stator slots. *Machines* **2022**, *10*, 1143. [CrossRef]
44. Premaratne, P.; Jawad-Kadhim, I.; Qadim-Abdullah, M.; Halloran, B.; James-Vial, P. A survey on low speed low power axial flux generator design and optimization using simulation. *Neurocomputing* **2022**, *509*, 272–289. [CrossRef]
45. Petrov, I.; Niemel, M.; Ponomarev, P.; Pyrhönen, J. Rotor surface ferrite permanent magnets in electrical machines: Advantages and limitations. *IEEE Trans. Ind. Electron.* **2017**, *64*, 5314–5322. [CrossRef]
46. Hong, J.; Park, S.; Hyun, D.; Kang, T.J.; Lee, S.B.; Kral, C.; Haumer, A. Detection and classification of rotor demagnetization and eccentricity faults for PM synchronous motors. *IEEE Trans. Ind. Appl.* **2012**, *48*, 923–932. [CrossRef]
47. Jeong, J.; Lee, H.; Orviz, M.; Lee, S.B.; Reigosa, D.; Briz, F. Detection of trailing edge PM demagnetization in surface PM synchronous motors. *IEEE Trans. Ind. Appl.* **2023**, *59*, 3390–3399. [CrossRef]
48. Joksimović, G.; Zajec, P.; Tessarolo, A.; Ambrožič, V.; Rihar, A. Stator Current Spectral Content of Inverter-Fed Cage Rotor Induction Motor. *IEEE Access* **2022**, *10*, 23112–23121. [CrossRef]
49. Xu, Y.; Xu, Z.; Ai, M. Application of Ring Winding in Induction Motor. *IEEE Trans. Appl. Supercond.* **2021**, *31*, 0603705. [CrossRef]
50. Antonino-Daviu, J.A.; Quijano-Lopez, A.; Rubbiolo, M.; Climente-Alarcon, V. Advanced analysis of motor currents for the diagnosis of the rotor condition in electric motors operating in mining facilities. *IEEE Trans. Ind. Appl.* **2018**, *54*, 3934–3942. [CrossRef]
51. Climente-Alarcon, V.; Antonino-Daviu, J.A.; Strangas, E.G.; Riera-Guasp, M. Rotor-bar breakage mechanism and prognosis in an induction motor. *IEEE Trans. Ind. Electron.* **2014**, *62*, 1814–1825. [CrossRef]
52. Sizov, G.Y.; Sayed-Ahmed, A.; Yeh, C.C.; Demerdash, N.A. Analysis and diagnostics of adjacent and nonadjacent broken-rotor-bar faults in squirrel-cage induction machines. *IEEE Trans. Ind. Electron.* **2009**, *56*, 4627–4641. [CrossRef]
53. Korman, O.; Degano, M.; Di Nardo, M.; Gerada, C. A Novel Flux Barrier Parametrization for Synchronous Reluctance Machines. *IEEE Trans. Energy Convers.* **2021**, *8969*, 675–684. [CrossRef]
54. Kim, H.; Park, Y.; Oh, S.T.; Jeong, G.; Seo, U.J.; Won, S.H.; Lee, J. Study on Analysis and Design of Line-Start Synchronous Reluctance Motor Considering Rotor Slot Opening and Bridges. *IEEE Trans. Magn.* **2022**, *58*, 1–6. [CrossRef]
55. Gallardo, C.; Madariaga, C.; Tapia, J.A.; Degano, M. A Method to Determine the Torque Ripple Harmonic Reduction in Skewed Synchronous Reluctance Machines. *Appl. Sci.* **2023**, *13*, 2949. [CrossRef]
56. Ban, B.; Stipetic, S. Systematic metamodel-based optimization study of synchronous reluctance machine rotor barrier topologies. *Machines* **2022**, *10*, 712. [CrossRef]
57. Navarro-Navarro, A.; Ruiz-Sarrio, J.E.; Biot-Monterde, V.; Antonino-Daviu, J.A.; Becker, V.; Urschel, S. Application of transient analysis techniques to fault diagnosis in Low-and medium-power synchronous machines. *Machines* **2023**, *11*, 288. [CrossRef]
58. Murataliyev, M.; Degano, M.; Di Nardo, M.; Bianchi, N.; Gerada, C. Synchronous reluctance machines: A comprehensive review and technology comparison. *Proc. IEEE* **2022**, *110*, 382–399. [CrossRef]
59. Pryhönen, J.; Jokinen, T.; Hrabovcová, V. *Design of Rotating Electrical Machines*; John Wiley & Sons: Chichester, UK, 2014.
60. Bramerdorfer, G.; Tapia, J.A.; Pyrhönen, J.J.; Cavagnino, A. Modern Electrical Machine Design Optimization: Techniques, Trends, and Best Practices. *IEEE Trans. Ind. Electron.* **2018**, *65*, 7672–7684. [CrossRef]
61. Cavagnino, A.; Bramerdorfer, G.; Tapia, J.A. Optimization of Electric Machine Designs—Part I. *IEEE Trans. Ind. Electron.* **2017**, *64*, 9716–9720. [CrossRef]
62. de la Barrera, P.M.; Otero, M.; Schallschmidt, T.; Bossio, G.R.; Leidhold, R. Active Broken Rotor Bar Diagnosis in Induction Motor Drives. *IEEE Trans. Ind. Electron.* **2021**, *68*, 7556–7566. [CrossRef]
63. Madariaga-Cifuentes, C.; Ruiz-Sarrio, J.E.; Antonino-Daviu, J.A.; Gallardo, C.; Tapia, J.A. Broken Bar Detection of Axial-Flux Induction Machines Through Advanced Transient Current Signature Analysis. In Proceedings of the 2024 International Conference on Electrical Machines (ICEM), Torino, Italy, 1–4 September 2024; pp. 1–6.

64. Ullah, Z.; Lee, S.-T.; Siddiqi, M.R.; Hur, J. Online Diagnosis and Severity Estimation of Partial and Uniform Irreversible Demagnetization Fault in Interior Permanent Magnet Synchronous Motor. In Proceedings of the 2019 IEEE Energy Conversion Congress and Exposition (ECCE), Baltimore, MD, USA, 29 September–3 October 2019; pp. 1682–1686.
65. Candelo-Zuluaga, C.; Riba, J.-R.; Thangamuthu, D.V.; Garcia, A. Detection of Partial Demagnetization Faults in Five-Phase Permanent Magnet Assisted Synchronous Reluctance Machines. *Energies* **2020**, *13*, 3496. [CrossRef]
66. Lopez, C.A.; Babel, A.S.; Strangas, E.G. Detecting uniform and partial demagnetization for an interior permanent magnet machine. In Proceedings of the 2016 XXII International Conference on Electrical Machines (ICEM), Lausanne, Switzerland, 4–7 September 2016; pp. 2874–2880.
67. Liang, P.; Tang, Y.; Chai, F.; Shen, K.; Liu, W. Calculation of the Iron losses in a Spoke-Type Permanent Magnet Synchronous In-Wheel Motor for Electric Vehicles by Utilizing the Bertotti Model. *IEEE Trans. Magn.* **2019**, *55*, 1–7. [CrossRef]

Disclaimer/Publisher's Note: The statements, opinions and data contained in all publications are solely those of the individual author(s) and contributor(s) and not of MDPI and/or the editor(s). MDPI and/or the editor(s) disclaim responsibility for any injury to people or property resulting from any ideas, methods, instructions or products referred to in the content.